Journal of Chemical and Petroleum Engineering (JChPE)
Print ISSN: 2423-673X Online ISSN: 2423-6721

Investigation of Finned Tubes Failure in the Furnace of Dehydration Unit at 10th Refinery of South Pars Gas Complex

Mohammad Hossein Farghadin [a] *, **Mohammad Nemati** [b], **Reza Mosayebi** [a]

[a] Technical Inspection Department, South Pars Gas Complex, 10th Refinery, Kangan, Iran.
[b] Management Department, South Pars Gas Complex, 10th Refinery, Kangan, Iran.

ARTICLE INFO

Article History:
Received: 13 October 2025
Revised: 08 December 2025
Accepted: 21 April 2026
Published: 21 April 2026

Article type: Research

Keywords:
Chromium Carbide,
Crack,
FE-SEM,
Sulfidation,
Thermal Transfer Coefficient,
XRD

ABSTRACT

Finned tubes are widely used in the convection sections of industrial furnaces to enhance heat transfer efficiency. However, their service life can be limited by thermal, mechanical, and chemical degradation mechanisms, particularly in high-temperature environments where dissimilar materials are employed. This paper focuses on the investigation of finned tube failures observed in the convection section of the dehydration furnace (Unit 104). The tubes were manufactured from ASTM A106 Grade B carbon steel, and the fins from AISI 304 stainless steel. To identify the root causes of failure, several experimental techniques were employed, including optical microscopy, Field emission scanning electron microscopy (FE-SEM), X-ray diffraction (XRD), X-ray fluorescence (XRF), and corrosion testing in accordance with ASTM A262-15 (2021) Practice A. Visual inspections revealed multiple cracks on both tube and fin surfaces. The analyses indicated that sulfide formation on fin surfaces, welding imperfections at the fin–tube interface, and differences in heat transfer coefficients between the two materials contributed to uneven thermal distribution and crack initiation. Furthermore, microstructural examination revealed chromium carbide precipitation and sensitization along grain boundaries in the fin material. The combined effects of these factors promoted crack propagation from the fins into the tube wall, ultimately leading to leakage and fire hazards.

Introduction

Natural gas is an essential energy source and a natural fuel found in oil and gas fields, along with impurities that have a high heating value. Water in both liquid and vapor form is known to be one of the most critical impurities in gas [1]. Vapor in natural gas can form hydrates, leading to pipeline blockages [2]. Reduced line capacity due to water accumulation in the line, and the increased risk of damage to pipelines and equipment from the corrosive effects of water, are other reasons for removing vapor from the natural gas stream [3]. Natural gas moisture must be kept below a set threshold to meet water-dew-point limits before entering pipelines [4, 5]. Gas dehydration involves removing vapor from the gas stream by lowering the water temperature to its dew point and using adsorption beds. Molecular sieves are used in adsorption beds, which are one of the most important materials used as drying agents in natural gas dehydration [2, 4].

* Corresponding Authors: M.H. Farghadin (E-mail address: m.farghadin@nigc-spgc.ir)

Journal of Chemical and Petroleum Engineering, 2026, 60(1): 163-181.
Publisher: University of Tehran Press *DOI: 10.22059/jchpe.2026.403582.1675*

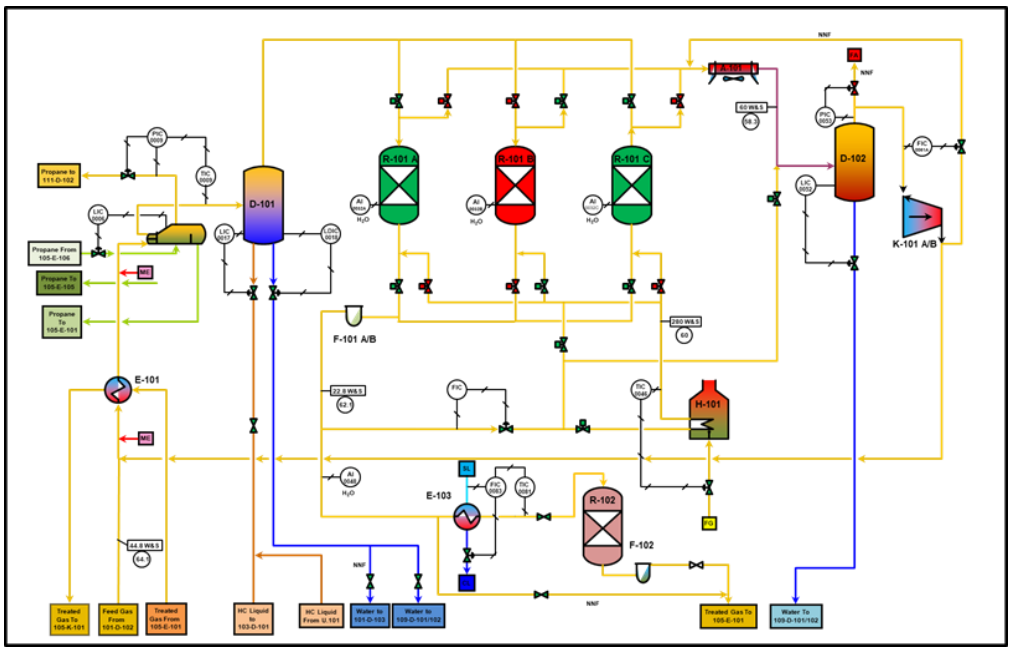

Fig. 1. View of unit 104 of the 10th refinery

The total capacity of the onshore facilities of the 10th refinery of the South Pars gas complex is 50 million cubic meters per day, and the main part of the operation, gas purification, is carried out in four parallel gas rows. After being sweetened by amine, the gas entering the gas rows passes through the dehydration unit (Unit 104), where its dew point is lowered to –95 °C and the water content is reduced to approximately 0.1 ppm. The natural gas dehydration system at the 10th South Pars refinery uses molecular sieve beds (3–5 mm at the bottom, 2–3 mm at the top) with activated alumina in the upper section. A view of the process used in the dehydration unit of the 10th refinery is shown in Fig. 1. The solid adsorption dehydration system has advantages over liquid adsorption, such as the possibility of reaching very low dew points, low sensitivity to changes in temperature, pressure, and gas flow rate, relative ease of operation and design of the units, and the insignificance of corrosion and foaming issues in them [4]. In this system, two beds are absorbing, and the third bed is regenerating. The furnace is a vital and effective piece of equipment in the hot-gas regeneration section [6, 7]. A view of the furnace of the dehydration unit is shown in Fig. 2.

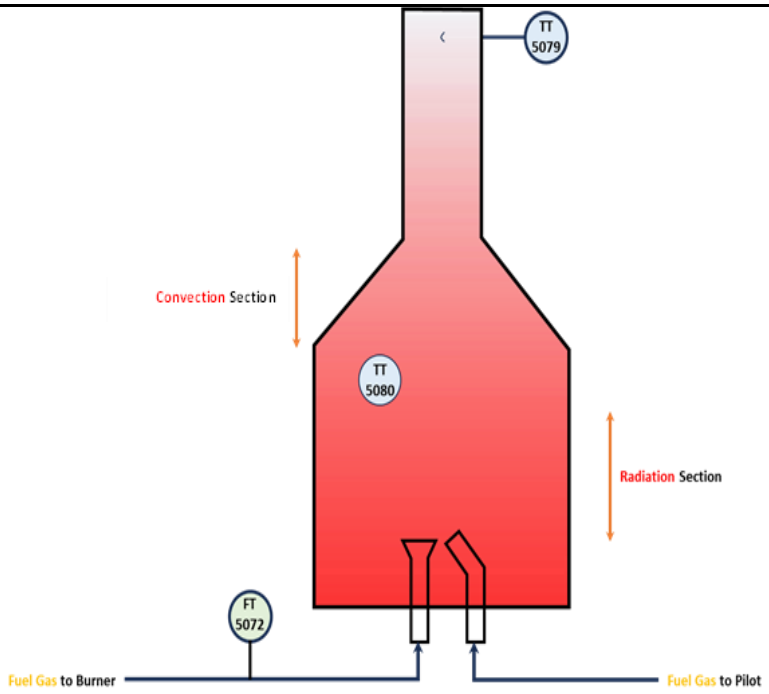

Fig. 2. Schematic of the unit 104 furnace

The efficiency of the convection section of the second-row furnace at the 10th refinery's second row fell from about 34% at the start of commissioning in 2017 to below 20% over time, as shown in Fig. 3.

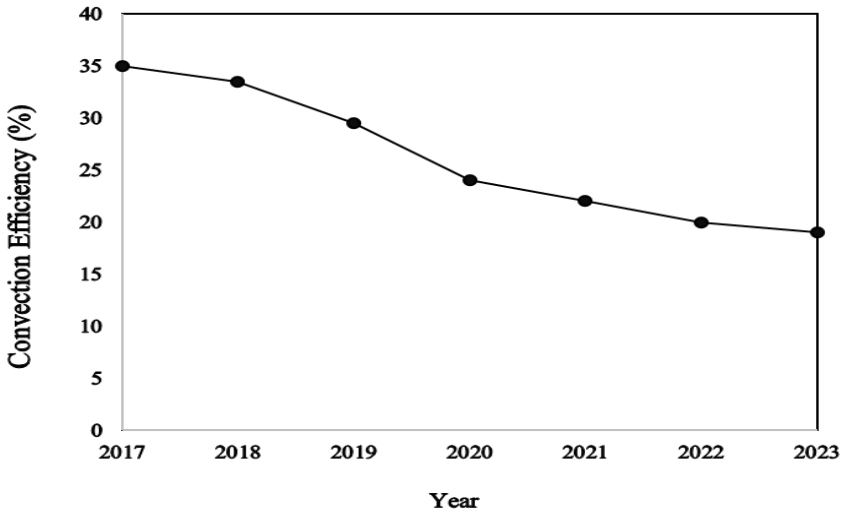

Fig. 3. Declining trend in efficiency of the convection section of the boiler

Zeng et al. conducted a comprehensive review of both open-source and proprietary databases to enhance the mechanistic understanding of corrosion processes in fuel-gas component materials used in existing fuel combustion systems [8]. Their work also aimed to identify potential alloy candidates suitable for the construction of flue gas components in high-pressure oxy-combustion technologies, thereby contributing to material selection strategies for next-generation combustion plants. Rojacz et al. examined the corrosive atmosphere in high-temperature environments for various alloyed steels and reported that even austenitic heat-resistant steels exhibit inadequate corrosion protection [9]. This deficiency was attributed to the formation of two distinct oxide scales—one enriched in Fe–Ni and the other in Fe–Cr—which leads to reduced oxidation resistance and scale instability at elevated temperatures. The formation of deposits on both the Radiation and Convection sections is inevitable. The

composition of deposits can vary depending on fuel type in the furnaces [10]. In the case of the furnaces of the 10th Refinery's dehydration unit, these deposits include FeS, Fe_2O_3, Fe_3O_4, polymers, refractory materials, dust and soot, compounds resulting from the combustion of fuel, air, and sulfur. These deposits form on the outer walls of the process pipes. These deposits can be very sticky, and as their thickness increases, the temperature of the pipe's outer wall must rise to keep the process fluid temperature constant. If the thickness increases further, the temperature may exceed the allowable design limit for the pipe, which is about 475 °C for carbon steel. The metal structure will disintegrate, and the pipe will burst. One of the most effective ways to enhance heat transfer rate and heat transfer coefficient in a relatively small volume is the use of finned tubes, which are manufactured in various types depending on the specific application [4, 11]. Increasing the number of fins along a given tube length improves efficiency. When two materials with different heat transfer coefficients are used, heat tends to accumulate in the material with the lower coefficient [10, 12]. Also, an improper connection between the fin and the tube causes impurities to accumulate in the unconnected regions, leading to poor or uneven heat transfer [13].

As a result, due to the cases mentioned above, the fin surface temperature increases unintentionally [14, 15]. Excessive temperature rise in stainless steels leads to the accumulation of carbon at the grain boundaries. This carbon combines with chromium at the boundaries to form chromium carbide, reducing chromium and initiating grain boundary corrosion [14, 16]. Jelani et al. examined a stainless-steel tube from an industrial furnace. They revealed that the formation of brittle compounds significantly lowered the material's impact strength, thereby increasing its susceptibility to brittle fracture under operational stresses [17]. Xiao et al. investigated failures of convection section tubes in an ethylene cracking furnace. They found that overheating caused cracking of the protective oxide film, with corrosion products composed mainly of metal oxides and carbides [18]. High tube temperatures and sulfide compounds in the feed can cause sulfidation along grain boundaries, leading to tube and fin failure. Root cause analysis is an effective method for investigating such material failures [19-21]. Despite extensive research on high-temperature corrosion, the combined impact of deposit accumulation, thermal conductivity mismatches, and fin-to-tube connection flaws on the long-term performance of finned tubes in real industrial settings remains unexplored. This study shows that deposit accumulation, thermal conductivity mismatches, and fin-to-tube connection defects are the primary causes of localized overheating, grain boundary corrosion, and finned-tube failure in natural gas dehydration furnaces, offering guidance for designing safer, higher-performance industrial furnaces. In this study, it is assumed that finned tube failures in gas industry furnaces may result from several degradation mechanisms. These include overheating, which can weaken the material under high furnace temperatures; erosion corrosion, caused by the combined effect of high-velocity flue gases and corrosive components; corrosion fatigue, resulting from cyclic thermal and mechanical loads in a corrosive environment; thermal fatigue, due to repeated heating and cooling cycles of the tubes; and stress corrosion cracking, which may develop under tensile stresses in the presence of corrosive species.

These mechanisms are considered key assumptions in evaluating the reliability and service life of finned tubes in industrial furnace conditions. By examining all aspects, including material quality, design errors, manufacturing errors, etc., similar failures can be prevented in the future. Due to using finned tubes (tubes regarding to ASTM A106 Grade B and fins regarding to AISI 304) in the convection section of the Unit 104 furnace to increase the temperature of the process gas inside the tubes through the heat generated by combustion, and after about 6 years of operation of the furnace and the occurrence of various thermal cycles with process gas leakage from the tubes to the convection section, the furnace caught fire and was

out of operation. By organizing a root cause investigation team to prevent a similar incident in other furnaces, samples of the affected parts were prepared and sent to the laboratory for testing, including FE-SEM, XRF, and optical microscope imaging.

Materials and Methods

To investigate the failure, one sample of the damaged finned tube was collected and sent to the laboratory for analysis. First, an emission spectrometry test was performed in accordance with ASTM A751 to determine the chemical composition of the tube and the fin. Also, hardness and tensile tests were performed separately at ambient temperature on the tube and fin in accordance with the A370 standard. XRF tests were performed in accordance with the ASTM E1621 standard, and XRD tests were performed on the deposits on the inner part of the tube in accordance with the BS EN 13925-2 standard. Using a 2% Nitel solution, glycyrrhizin, and oxalic acid, the microscopic surfaces of the tube and fin in the fracture area were examined, respectively. To investigate the alloy's sensitivity to grain boundary corrosion, in accordance with ASTM A262-15 Practice A, the sample was evaluated for 1.5 minutes in a 10% oxalic acid solution under a current of 1 A/cm2. Using a FESEM microscope, the fracture surfaces in the tube and fin sections, as well as the existing deposits, were examined more closely using EDS testing.

Results and Discussion

Visual Observations

Visual Evaluation of the tube was performed by determining four hypothetical positions: 3, 6, 9, and 12 o'clock. There are some colorful deposits on the inner tube side. At the hypothetical position 12-3 and 3-6 o'clock (Fig. 4a & b) brown and black products are clearly seen, also at the hypothetical position 6-9 o'clock (Fig. 4c) only black products are observed besides shallow holes, however only at the hypothetical position 6 o'clock, radial cracks are observed in the fins along the tube (Fig. 4). Also, the cracks in the tube and the radial cracks in the fin section are connected (Fig. 5). Considering the connection of the cracks in the fin and tube and their alignment, there is a possibility that the origin of the crack initiation is the same in both.

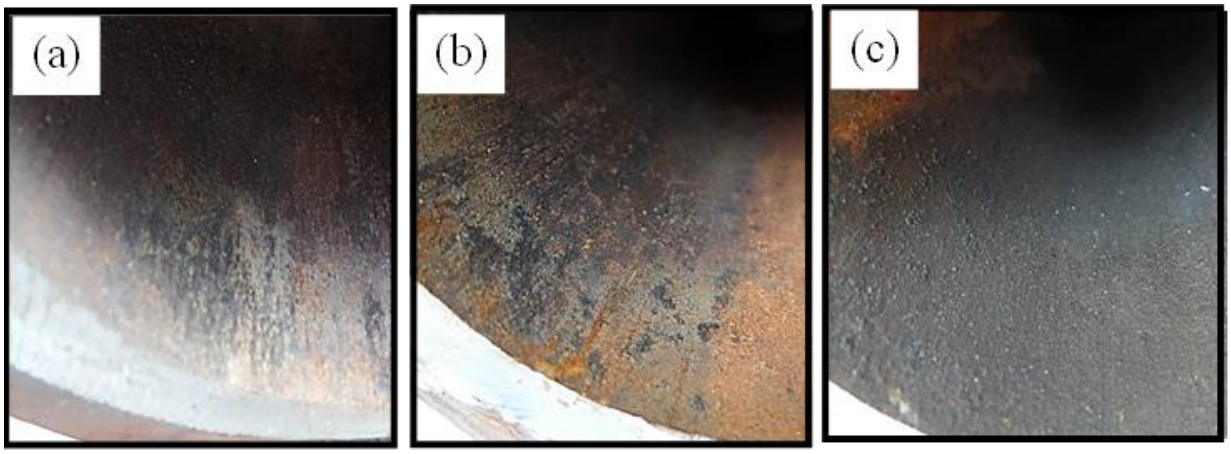

Fig. 4. Formation of deposits at (a) 12-3 o'clock, (b) 3-6 o'clock, and (c) 6-12 o'clock hypothetical positions

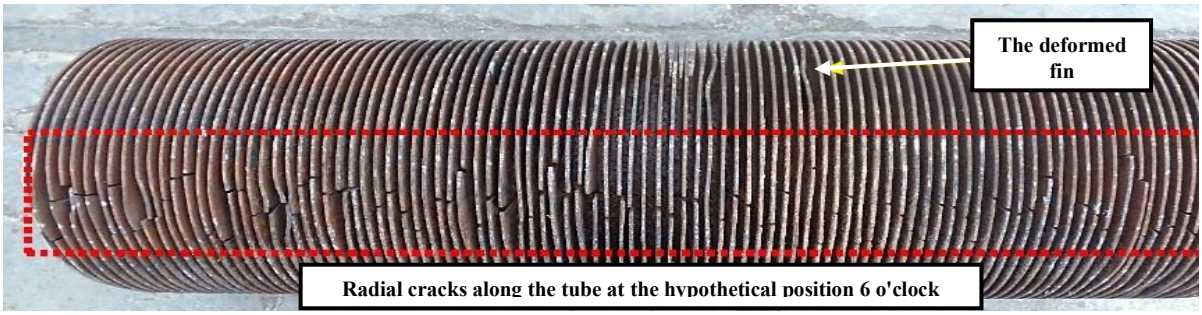

(a)

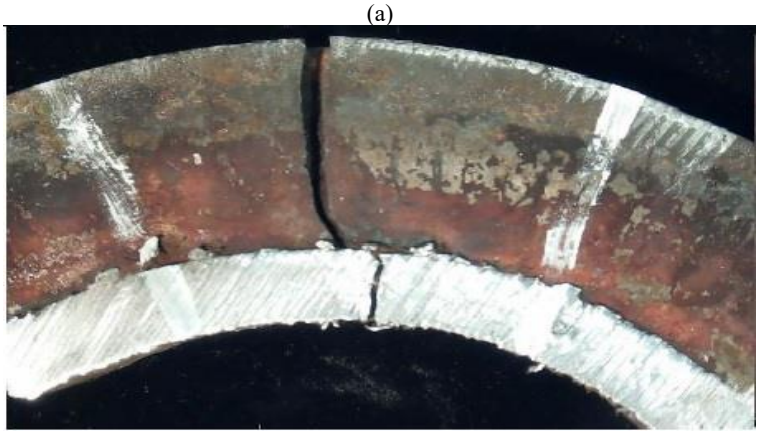

(b)

Fig. 5. (a) Radial cracks on the fin, and (b) crack propagation in both the tube and the fin

Chemical Analysis

Tube

By examining the chemical composition of the pipe using emission spectrometry (Table 1), the percentage of all elements is within the permissible range of the ASTM A106 standard for Grade B.

Table 1. The tube's chemical composition

Element	C	Si	Mn	P	S	Cr	Mo
Composition (wt%)	0.16	0.21	0.72	0.016	< 0.003	0.20	0.07
Element	V	W	Pb	Sn	B	Zr	Bi
Composition (wt%)	0.002	< 0.015	< 0.01	0.006	< 0.0008	< 0.002	< 0.01
Element	Ni	Al	Co	Cu	Nb	Ti	
Composition (wt%)	0.09	0.013	0.01	0.16	0.005	< 0.002	
Element	As	Fe	Cr + Cu + Ni + Mo + V	CE			
Composition (wt%)	< 0.004	Base	0.52	0.35			

Fin

By examining the chemical composition of the fin by emission spectrometry (Table 2), the percentage of all elements is within the permissible range of the ASTM A240 standard for Grade 304.

Table 2. Chemical analysis results from the fin

Element	C	Si	Mn	P	S	Cr	Mo	Ni	Al	Co	Cu
Composition (wt%)	0.05	0.36	1.07	0.024	0.008	18.1	0.31	8.3	< 0.005	0.26	0.27
Element	Nb	Ti	V	W	Pb	Sn	Zr	Se	N	Fe	
Composition (wt%)	0.012	0.012	0.07	0.04	Trace	0.007	< 0.005	Trace	0.08	Base	

Hardness test

The Brinell hardness test was performed at the center of the pipe cross-section at 3, 6, 9, and 12 o'clock, as well as at the center of one of the fins welded to the pipe (Tables 3 & 4). The results obtained are within the acceptable range of the ASTM A106 standard for Grade B and the ASTM A240 standard for Grade 304**.**

Table 3. The tube hardness test results

Row	**Hardness testing position**	**Hardness number at measured points (HBW)**			**Average hardness number (MBW)**
		Point 1	**Point 2**	**Point 3**	
1	3 O'clock	143	144	142	143
2	6 O'clock	146	142	144	144
3	9 O'clock	141	143	145	143
4	12 O'clock	140	141	145	142

Table 4. The fin hardness test results

Hardness testing position	**Applied force (Kgf)**	**Hardness number at measured points (HBW)**			**Average hardness number (HBW)**	**Hardness limit in terms of HBW based on A240 standard for Grade 304**
		Point 1	**Point 2**	**Point 3**		
Center of the sample	187.5	189	187	183	186	Max 201

Tensile Test at Ambient Temperature

According to the tensile test results at ambient temperature for the pipe at positions 6 and 12 (Table 5) and a review of the values in the ASTM A240 Grade B standard, the pipe properties meet the allowable limits of the standard.

Table 5. Tensile test results of the tube in two different positions at ambient temperature

Position	**Thickness*Width (mm*mm)**	**Cross-section (mm^2)**	**Yield strength Rt (MPa)**	**Ultimate strength Rt (MPa)**	**Relative elongation $\%A_{50}$**
12 O'clock	12.45*7.4	92.13	330	505	33
6 O'clock	12.45*7.25	90.26	333	500	34
Permissible limits according to the ASTM A106 Grade B standard			Min 240	Min 415	Min 21

Emission spectrometry results indicate that the chemical composition of the fin and tube material falls within the standard limits, confirming its satisfactory quality. Hardness and tensile tests confirm that the fin and tube material meet standard specifications, demonstrating acceptable mechanical and manufacturing quality.

XRF

The weight percentages of various compounds on the internal and external surfaces of the pipe were determined by XRF testing, and the results are presented in Tables 6 & 7. Also, due to oxidation and the presence of sulfide compounds in the refinery input feed, the main compounds on the inner surface are Fe2O3 and SO2 + S, and those on the outer surface are Fe_2O_3 and SO_3.

Table 6. Compounds extracted by XRF on the tube external side

Compound	Na_2O	SO_3	Cr_2O_3	ZnO	PbO	MgO		
Composition (wt%)	0.5	34.4	1.6	< 0.01	< 0.01	0.8		
Compound		SrO	La & Lu	SiO_2	TiO_2	NiO		
Composition (wt%)		< 0.01	< 0.01	8.0	0.3	< 0.01		
Compound		K_2O	MnO_2	As_2O_3	L.O.I	Al_2O_3	CaO	Fe_2O_3
Composition (wt%)		0.9	0.2	< 0.01	7.5	2.7	24.3	18.8
Compound		ZrO_2	P_2O_5	V_2O_5	CuO	BaO		
Composition (wt%)		< 0.01	< 0.01	< 0.01	< 0.01	< 0.01		

Table 7. XRF test result of the inner surface of the tube

Compound	Na_2O	SO_2 + S	Cr_2O_3	ZnO	PbO	MgO	K_2O
Composition (wt%)	0.3	8.1	0.5	0.2	< 0.01	0.5	0.2
Compound	SrO	La & Lu	SiO_2	TiO_2	NiO	ZrO_2	P_2O_5
Composition (wt%)	< 0.01	0	4.8	< 0.01	< 0.01	< 0.01	< 0.01
Compound	MnO_2	As_2O_3	L.O.I	Al_2O_3	CaO	Fe_2O_3	
Composition (wt%)	0.5	< 0.01	0	1.7	5.0	77.9	
Compound	V_2O_5	CuO	BaO				
Composition (wt%)	< 0.01	0.3	< 0.01				

XRD

XRD analysis of deposits on the inner and outer pipe surfaces, conducted in accordance with BS EN 13925-2, identified various compounds, including pyrrhotite, quartz, and hematite (Table 8).

Table 8. Deposits obtained by XRD on the tube's internal and external sides

External surface deposits	
Chemical formula	**Chemical composition**
$CaSO_4.2H_20$	Gypsum
$CaSO_4$	Anhydrite
Fe_3O_4	Hematite
SiO_2	Quartz
Fe_2O_3	Magnetite
$CaCO_3$	Calcite
$KFe_3(FeSi_3)O_{10}(OH)_2$	Annite (Minor)
$Fe_{43.96}Ni_{4.00}S_{49.00}$	Pyrrhotite
FeS	Iron sulfide

According to the XRF and XRD results, the presence of oxide products such as Fe2O3 and CaO confirms the oxidation process; these two compounds are prominent oxides according to the XRF results. Furthermore, sulfide products such as FeS, $CaSO_4$, and SO_3 were formed due to contact of the fluid and the tube. The sulfide compounds detected on the inner and outer surfaces of the pipe likely resulted from H_2S in the gas stream and from combustion gases. (Tables 9 & 10). With regarding to Tables 6 & 7 on external side of the tube SO_4 34.4 wt%,

CaO 24.3 wt%, Fe_2O_3 18.8 wt%, SiO_2 8.0 wt%, and on inner side Fe_2O_3 77.9 wt%, SiO_2 4.8 wt%, and SO_2 + S 8.1 wt% are main products.

Table 9. Chemical composition of combustion fuel in three states

Fuel gas (normal) %mol	Fuel gas (design) %mol	Fuel gas (summer) %mol	Element
0.83	0.68	0.68	CO_2
3.66	3.81	3.81	N_2
89.69	93.39	93.43	Methane
5.73	2.04	2.01	Ethane
0.08	0.061	0.058	Propane
2.18 e^{-3}	2.3 e^{-3}	2.27 e^{-3}	I-Butane
1.61 e^{-3}	1.7 e^{-3}	1.68 e^{-3}	N-Butane
1.1 e^{-4}	1.13 e^{-4}	1.15 e^{-4}	C_5+
4.8 e^{-5}	5.0 e^{-5}	4.9 e^{-5}	Mercaptans
1.15 e^{-5}	2.3 e^{-5}	2.2 e^{-5}	CoS
3.1 e^{-4}	1.19 e^{-4}	1.17 e^{-4}	H_2S

Table 10. Chemical composition of the gas in the tube

Chemical composition	% Molar	Chemical composition	% Molar
H_2O	0.1 ppm mol	C_6 cut	0.1367
N_2	3.533	Benzene	100 ppm mol
CO_2	0.8004	C^{7+}	0.1325
H_{2S}	3 ppm mol	COS	4.2 ppm mol
Methane	86.5178	CH_4S	24.1ppm mol
Ethane	5.5294	ETSH	144 ppm mol
Propane	2.0393	PRITHIOL	6.0 ppm mol
I-Butane	0.3763	BUTHIOL	1.8 ppm mol
Butane	0.5776	HXITHIOL	900 ng/Nm^3
I-Pentane	0.1768	MERCURY	-
Pentane	0.1577	-	-

The tube's internal surface deposit structure was investigated by XRD analysis. Fig. 6 illustrates the XRD pattern of the tube's internal surface deposits. As shown in Fig. 6, two reference codes matched the detected peaks in the XRD pattern. Reference code JCPDS 969013705 for Fe-Ni-S compound ($Fe_{43.96}Ni_{4.00}S_{49.00}$) named Pyrrhotite with Monoclinic structure has seven detected peaks at diffraction angle 29.85°, 33.75°, 43.61°, 53.01°, 57.03°, 64.52°, 71.00° can be assigned to (025), (043), (046), (065), (228), ($\bar{4}$45), (086) crystallographic planes of the Fe-Ni-S compound respectively. Also, the peaks detected by JCPDS 961504401 reference code is about FeS with Hexagonal structure at the diffraction angle of 29.82°, 33.69°, 43.49°, 52.94°, 56.78°, 64.44°, 70.85° and 88.30° that could be related to (100), (101), (102), (110), (103), (004), (202) and (114) crystallographic planes. Based on the detected phases, it can be noted that the sulfide products have formed on the inner surface of the tube.

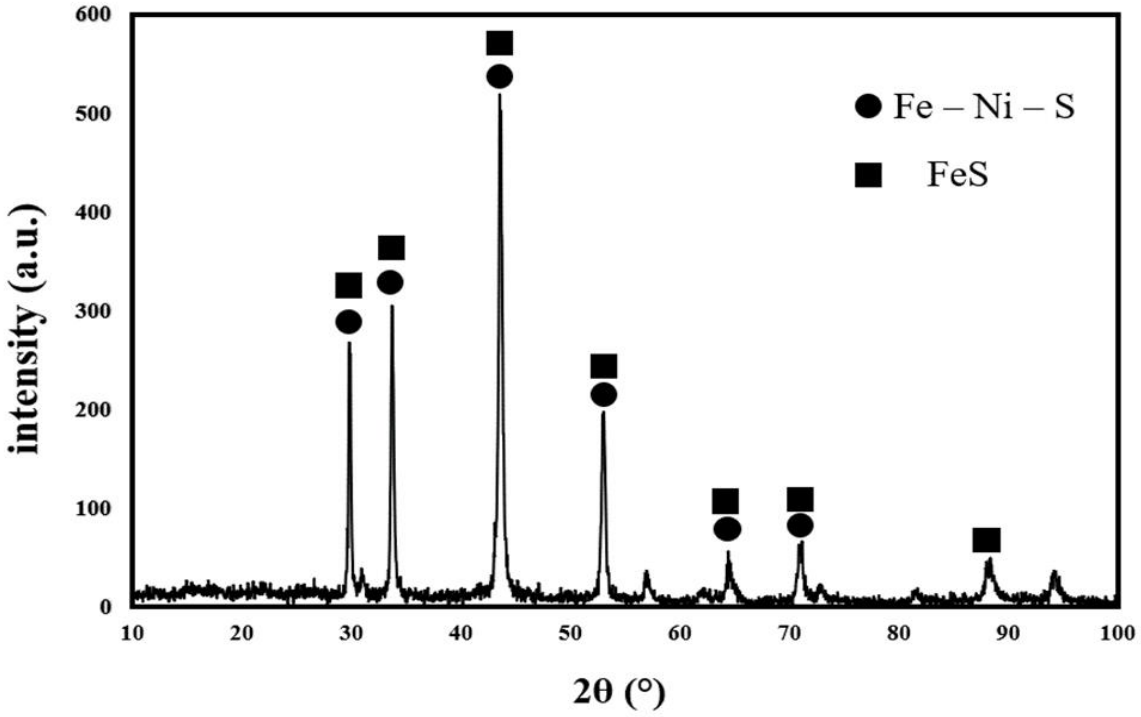

Fig. 6. XRD patterns of tube internal surface deposits

Microstructure Evaluations

Microscopic examination of the tube cross-section reveals the presence of multiple parallel cracks exhibiting both sharp and occasionally rounded (Fig. 7). First, by etching the boundary between the fin and the tube with 2% Nitrel solution, ferrite grains along with pearlite rows were visible in the tube structure. The cracks have grown intra-granularly in this part (Fig. 8). Also, microscopic defects were visible at the boundary of the fin-tube connection (Fig. 9). The heat-affected zone (HAZ) on the tube side predominantly comprises a ferritic matrix with a dispersed distribution of carbides and localized pearlitic regions. Microstructural analysis indicates that crack propagation occurred trans-granularly (Fig 10). The observed features are attributed to the high thermal input during welding and the absence of subsequent post-weld heat treatment (Table 11). The microscopic structure in this area has changed, transitioning from fine-grained to coarse-grained (Fig. 9), resulting in residual stresses in this region. The interaction between residual stresses and operational thermal stresses arising from the continuous exposure of these tubes to fluctuating thermal cycles can facilitate the detachment of the fin from the tube. Also, the coarse-grained area is prone to the initiation or propagation of other cracks into the tube. Therefore, improper welding and residual stresses are among the causes of microscopic defects at the fin-tube junction. It should be noted that, in some areas, the defective fin-tube junction is likely to deposit corrosion products (Fig. 11).

Regarding post-heat treatment, attention should be paid to the potential for sigma phase formation in 304 stainless steel [22]. Therefore, performing solution annealing at a temperature above the sigma-phase formation range (590–870 °C) can inhibit sigma-phase precipitation in the fin and promote microstructural refinement in the tube section from coarse-grained to fine-grained while simultaneously eliminating sensitized grain boundaries within the fin region.

Table 11. Fin to body connection process specifications

Weld layer (s)	Process	Filler met	Dim (mm)	Ampere (Range)	Kilo volt (Range)	Frequency (Ran) KHz	Preheat	Other	PWHT	Current
1	High frequency (HF)-hot forging bond	NA	NA	13-20	6.5-8.5	210-320	NA	Post cooling by water	NA	A.C.

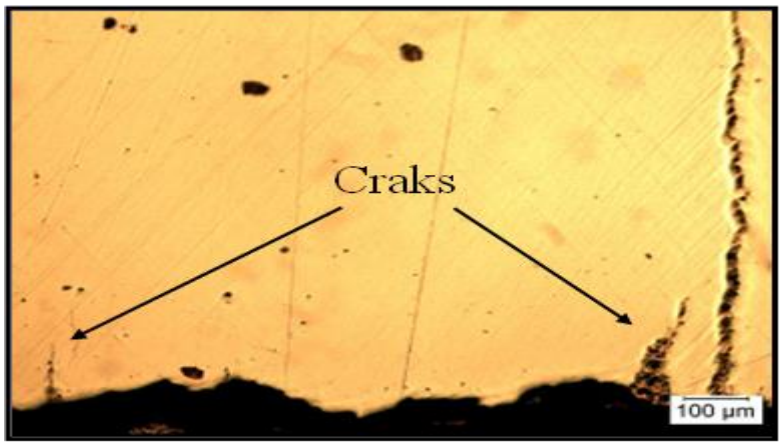

Fig. 7. Multiple microcracks with sharp points on the tube

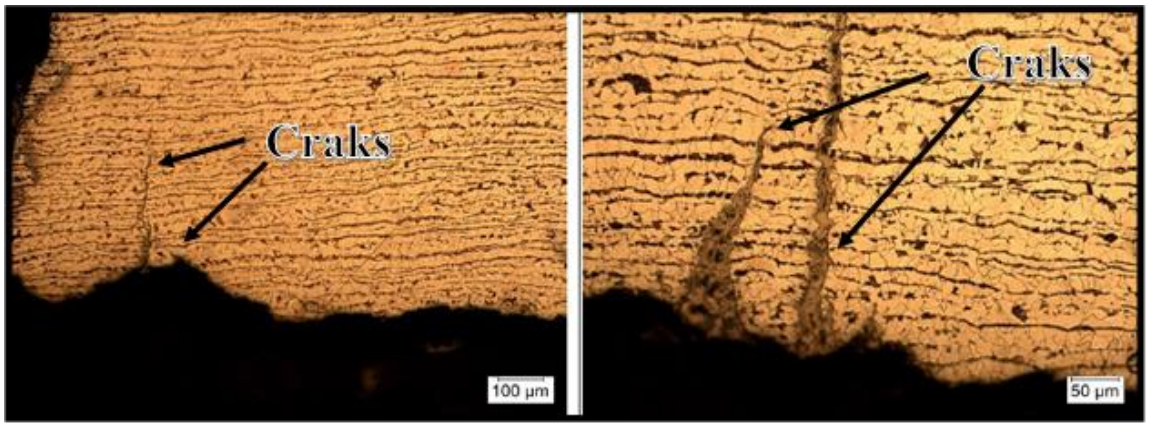

(a) (b)

Fig. 8. Crack propagation intra-granularly in the tube internal side at scale: (a) 100 µm, and (b) 50 µm

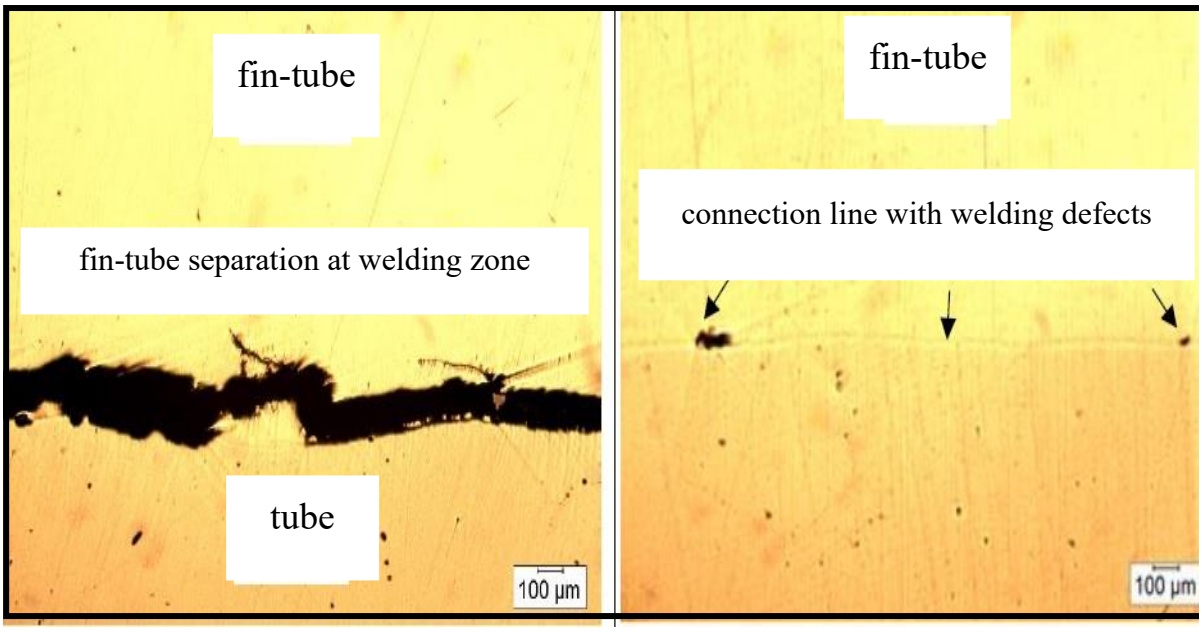

(a) (b)

Fig. 9. (a) Fin-tube separation at the welding zone, and (b) welding defects along the fin-tube connection line

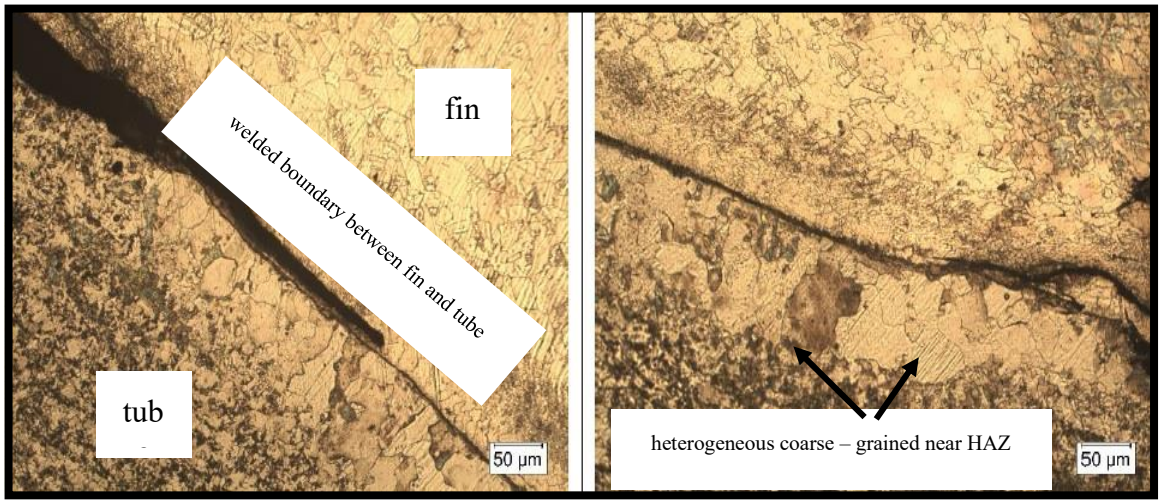

(a) (b)

Fig. 10. (a) Welded boundary between fin and tube, and (b) coarse-grained structure near the weld line

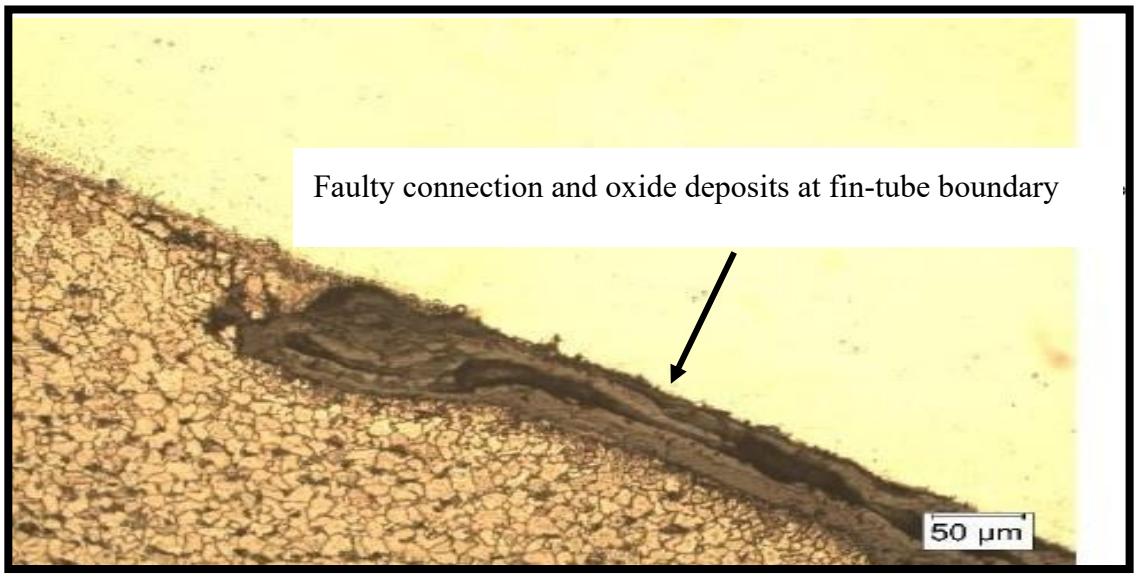

Fig. 11. Faulty connection at fin-tube boundary

Due to the difference in the heat transfer coefficient of the materials used in the fin and the tube (tube material: ASTM A106 grade B, fin material: AISI 304), the presence of numerous welding defects, and the accumulation of impurities among these defects, heat transfer from the fin surface to the tube has not taken place properly, and the fin surface has become the location of heat concentration (the fin surface temperature, according to field surveys, was in the range of 700 to 800 °C) [16]. This heat concentration in the fin creates difficulties, such as the formation of chromium carbide (at temperatures above 500 °C, the probability of its formation increases greatly) at grain boundaries. Afterward, due to a mismatch in the coefficients of thermal expansion and the localized heat distribution between the fin and tube, intergranular parallel cracks propagated toward the tube surface. This phenomenon is further attributed to the presence of chromium carbides within the fin region. These cracks are due to the coarse-grained structure in the weld area, which has weaker mechanical properties than the rest of the tube. The aforementioned cracks continued until they reached the tube's inner surface, after which leakage from the tube began, and a fire occurred. By etching the longitudinal section of the fin with glycyrrhizin solution and the transverse section of the fin with oxalic acid, austenite grains

with distribution of chromium carbide particles at the grain boundaries can be seen (Figs. 12 & 13). Also, cracks in the fin section were between grains, indicating steel sensitization (Fig. 14).

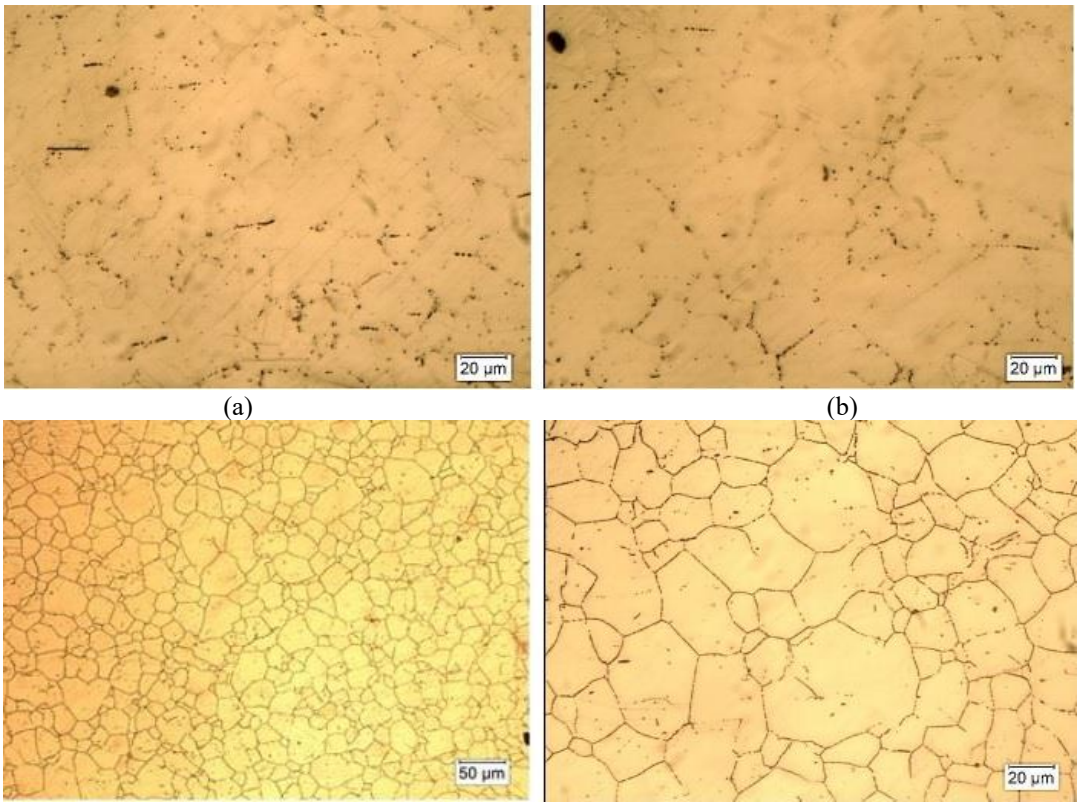

Fig. 12. (a & b) Longitudinal section of the fin, and (c & d) fin cross-section after etching

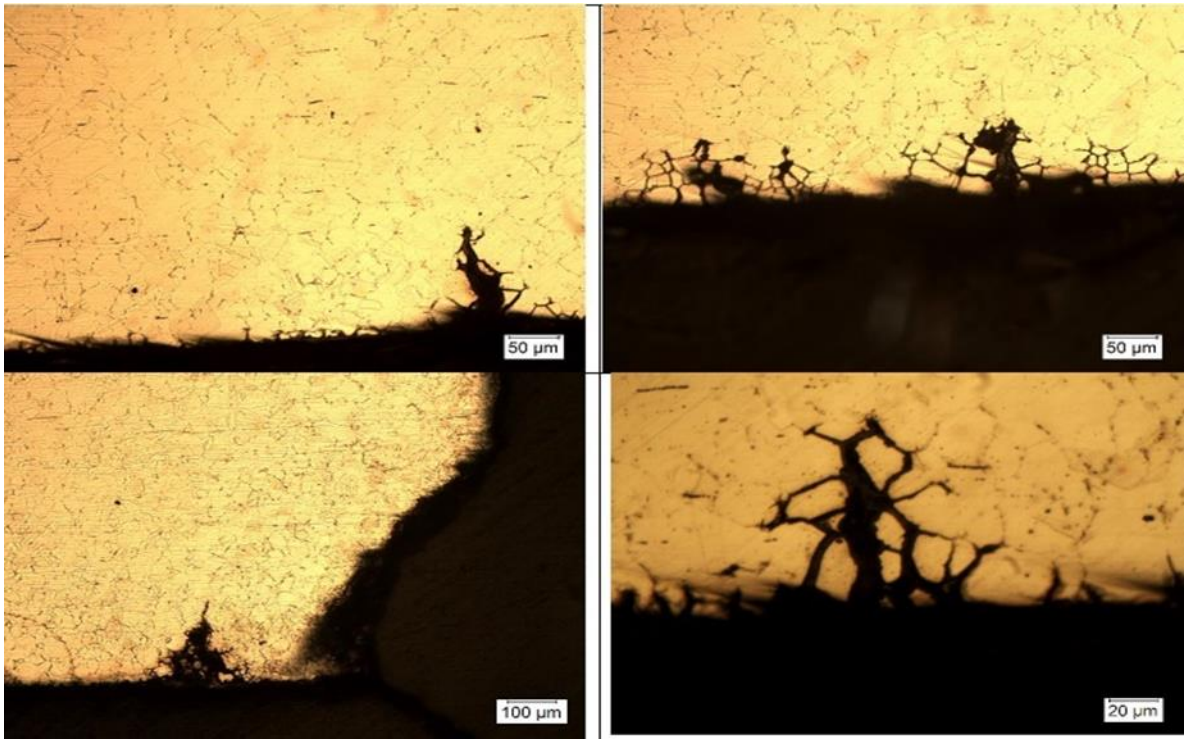

Fig. 13. Crack propagation in the fin section from the grain boundary at different scales

Grain Boundary Corrosion Test

Fig. 14 shows that, according to ASTM A262-15 Practice A, the fin surface is dual-structured, and its grain boundaries are sensitive and no longer resistant to grain boundary corrosion.

Fig. 14. Dual fin microstructure

FE-SEM

Fig. 15 is a longitudinal cross-section of the fin after etching, in which the growth of cracks between the grains can be seen.

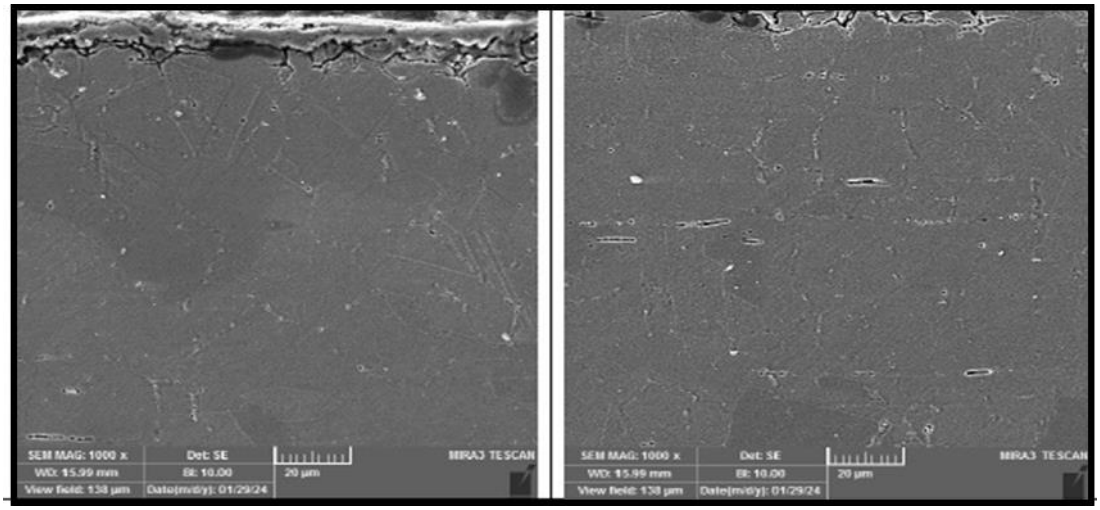

Fig. 15. Cracks propagation between the grains of the fin on two different sides

Sulfidation, also called sulfide corrosion, is a form of corrosion that occurs when sulfide compounds penetrate the alloy at high temperatures, leading to localized corrosion [23, 24]. According to the studies of the deposits in the cracks of the tube and the fin inner surface by energy dispersive X-ray spectroscopy (EDS test), the formation of sulfide and oxide compounds was quite evident. The presence of these compounds indicates sulfide corrosion and oxidation during crack propagation along the fin and tube surfaces, and a high percentage of Sulfur (S) confirms sulfidation (Fig. 16) [25, 26]. Based on the EDS extracted data, the Cl element is observed. Because of high humidity and proximity to the sea, the formation of chloride compounds is possible. High concentrations of iron, chromium, and sulfur, and the formation

of a sulfide phase, are evident in the EDS data (Fig. 17). The sulfidation on the fin surface indicates that the tube has been operating under service conditions in environments containing S and H_2S at high temperatures [27]. Fig. 17 shows that the deposit layer has penetrated the grain boundaries beneath the fin surface, and that cracks have spread into these grain boundaries [28].

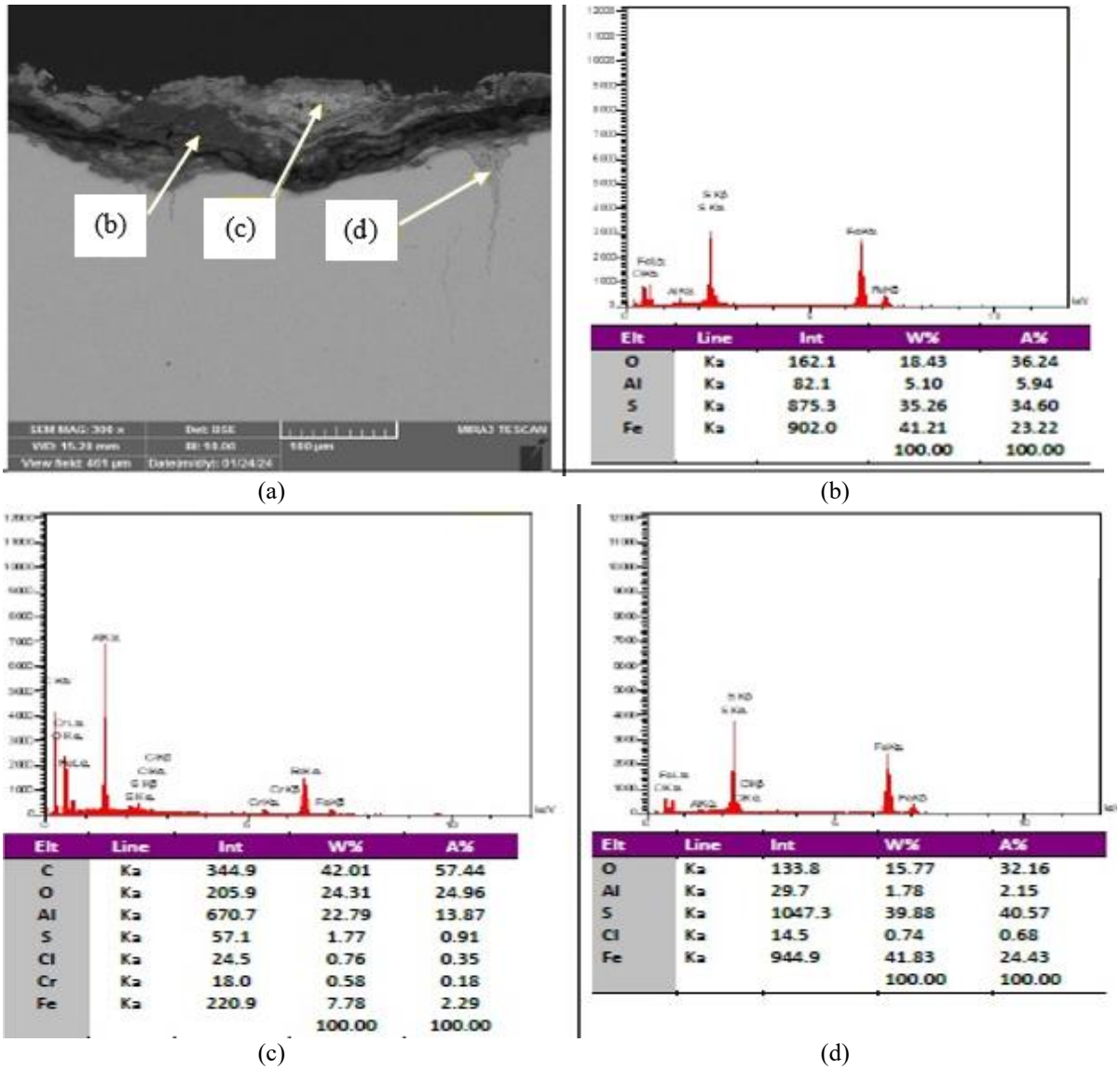

Elt	Line	Int	W%	A%
O	Ka	162.1	18.43	36.24
Al	Ka	82.1	5.10	5.94
S	Ka	875.3	35.26	34.60
Fe	Ka	902.0	41.21	23.22
			100.00	100.00

Elt	Line	Int	W%	A%
C	Ka	344.9	42.01	57.44
O	Ka	205.9	24.31	24.96
Al	Ka	670.7	22.79	13.87
S	Ka	57.1	1.77	0.91
Cl	Ka	24.5	0.76	0.35
Cr	Ka	18.0	0.58	0.18
Fe	Ka	220.9	7.78	2.29
			100.00	100.00

Elt	Line	Int	W%	A%
O	Ka	133.8	15.77	32.16
Al	Ka	29.7	1.78	2.15
S	Ka	1047.3	39.88	40.57
Cl	Ka	14.5	0.74	0.68
Fe	Ka	944.9	41.83	24.43
			100.00	100.00

Fig. 16. (a) FE-SEM image taken from the inner surface of the tube, and (b-d) EDS analyses of 3 random points

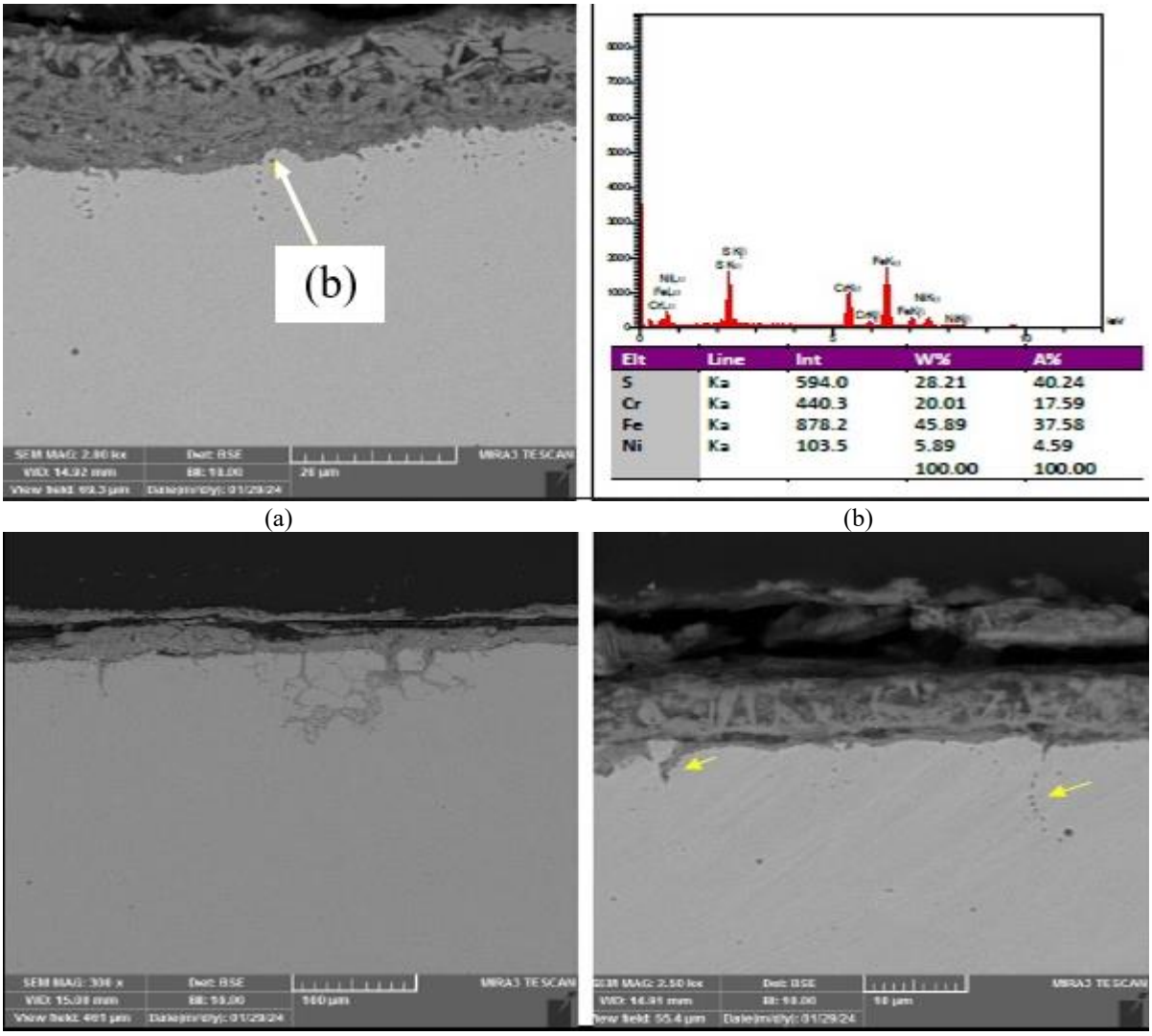

Fig. 19. (a) FE-SEM image taken from the inner surface of the fin surface, (b) EDS analysis of a random point, and (c & d) cross-section of the fin surface at two different scales

Conclusion

In this study, the reasons for the failure of the finned tubes of the Convection section of the dehydration furnace of Unit 104 of the 10th South Pars Refinery were investigated, and the results are summarized below:

• Based on visual inspections, all cracks occurred at the hypothetical 6 o'clock position, and the cracks in the fin and tube were not only aligned but also connected.

• Based on the results of emission spectrometry, hardness measurements, and tensile testing for both the tube and fin materials, and considering their conformity with the furnace manufacturer's material specifications, it can be concluded that the materials utilized in this section meet the required quality and comply with the relevant standards.

• After checking the results of the XRF and XRD tests, as well as examining the chemical composition of the fuel used in the furnace and the process gas inside the tube, there is a possibility of high-temperature oxidation and sulfidation processes.

• By examining the microscopic structure of the tube, in addition to the appearance of intra-grain crack growth, a coarse-grained HAZ structure is visible at the fin connection boundary.

• By evaluating the microscopic structure of the fin after etching, in addition to the grain boundary crack growth, the accumulation of chromium carbide at the grain boundary is also evident.

• Grain boundary corrosion sensitivity testing revealed that the grain boundaries exhibited insufficient resistance to intergranular corrosion.

• The results of the FESEM test show, besides the grain boundary crack growth in the fin section, there are some oxide and sulfide compounds in the inner part of the tube and on the fin surface, which confirms the occurrence of high-temperature oxidation and sulfidation processes.

• Owing to the difference in the heat transfer coefficient of the materials used in the fin and the tube, and faulty heat transfer from the fin surface to the tube, which results in heat concentration and formation of chromium carbide at the grain boundaries, crack propagation begins, which leads to failure.

• In austenitic stainless steel, high temperature (500 – 850 °C) and chromium carbide deposition along grain boundaries result in Cr depleted and Cr rich zones at grain boundaries, which leads to sensitization.

References

[1] P. Li, G. Wang, Y. Dong, Y. Zhuo, Y. Fan, A review on desulfurization technologies of blast furnace gases, Current Pollution Reports 8(2) (2022) 189–200. https://doi.org/10.1007/s40726-022-00212-z

[2] M.J. Jweeg, K.I. Mohammed, M.H. Tolephih, M. Al-Waily, Investigation into the distribution of erosion-corrosion in the furnace tubes of oil refineries, Materials Science Forum, Trans Tech Publ, 2021, pp. 165–181. https://doi.org/10.4028/www.scientific.net/MSF.1039.165

[3] G. Dak, S. Sirohi, C. Pandey, Study on microstructure and mechanical behavior relationship for laser-welded dissimilar joint of P92 martensitic and 304L austenitic steel, International Journal of Pressure Vessels and Piping 196 (2022) 104629. https://doi.org/10.1016/j.ijpvp.2022.104629

[4] T. Chen, L. Sun, Q. Li, C. Liu, Z. Liu, X. Cheng, X. Li, Comprehensive analysis of corrosion failure of blast furnace gas pipeline in a steel plant, Engineering Failure Analysis 154 (2023) 107651. https://doi.org/10.1016/j.engfailanal.2023.107651

[5] S. Papavinasam, R.W. Revie, W. I. Friesen, A. Doiron, T. Panneerselvan, Review of models to predict internal pitting corrosion of oil and gas pipelines, Corrosion Reviews 24(3-4) (2006) 173–230. https://doi.org/10.1016/j.engfailanal.2020.104505

[6] M. Mobaraki, B. Afshang, M. Rahimpour, M. Bahrololoom, A. Bolhasani, R. Davand, Effect of cracking feedstock on carburization mechanism of cracking furnace tubes, Engineering failure analysis 107 (2020) 104216. https://doi.org/10.1016/j.engfailanal.2019.104216

[7] I. Obot, I.B. Onyeachu, S.A. Umoren, M.A. Quraishi, A.A. Sorour, T. Chen, N. Aljeaban, Q. Wang, High temperature sweet corrosion and inhibition in the oil and gas industry: Progress, challenges and future perspectives, Journal of Petroleum Science and Engineering 185 (2020) 106469. https://doi.org/10.1016/j.petrol.2019.106469

[8] Y. Zeng, K. Li, R. Hughes, J.-L. Luo, Corrosion mechanisms and materials selection for the construction of flue gas components in advanced heat and power systems, Industrial & Engineering Chemistry Research 56(48) (2017) 14141–14154. https://doi.org/10.1021/acs.iecr.7b03664

[9] H. Rojacz, L. Krabac, M. Varga, K. Adam, G. Fafilek, High temperature corrosive environment in a sintering plant for pig iron production and its effect on different steel grades, steel research international 88(8) (2017) 1600431. https://doi.org/10.1002/srin.201600431

[10] M. Wasim, M.B. Djukic, External corrosion of oil and gas pipelines: A review of failure mechanisms and predictive preventions, Journal of Natural Gas Science and Engineering 100 (2022) 104467. https://doi.org/10.1016/j.jngse.2022.104467

[11] H. Ezuber, S. Zakir Hossain, A review of corrosion failures in shell and tube heat exchangers: roots and advanced counteractive, Heat and Mass Transfer 59(6) (2023) 971–987. https://doi.org/10.1007/s00231-022-03301-3

[12] A.H. Alamri, Localized corrosion and mitigation approach of steel materials used in oil and gas pipelines – An overview, Engineering Failure Analysis 116 (2020) 104735. https://doi.org/10.1016/j.engfailanal.2020.104735

[13] X. He, J. Wang, X. Lu, Q. Song, W. Su, Failure analysis on unexpected fracture of tube-to-tubesheet joints of a circulating oil steam generator, Engineering Failure Analysis 154 (2023) 107678. https://doi.org/10.1016/j.engfailanal.2023.107678

[14] G. Mubarak, C. Verma, I. Barsoum, A. Alfantazi, K.Y. Rhee, Internal corrosion in oil and gas wells during casings and tubing: Challenges and opportunities of corrosion inhibitors, Journal of the Taiwan Institute of Chemical Engineers 150 (2023) 105027. https://doi.org/10.1016/j.jtice.2023.105027

[15] A. Hajjari, T. Shahrabi, I. Mohammadi, Synthesis of a novel environmentally friendly hybrid pigment for effective corrosion control of mild steel, Journal of Environmental Chemical Engineering 11(2) (2023) 109383. https://doi.org/10.1016/j.jece.2023.109383

[16] A.R. Prasad, A. Kunyankandy, A. Joseph, Corrosion inhibition in oil and gas industry: Economic considerations, Corrosion inhibitors in the oil and gas industry (2020) 135–150. https://doi.org/10.1002/9783527822140.ch5

[17] A. Jelani, M.M. Butt, O.U. Rauf, Failure analysis of a furnace tube support, Engineering Failure Analysis 157 (2024) 107910. https://doi.org/10.1016/j.engfailanal.2023.107910

[18] S. Xiao, J. Wang, C. Huang, L. Tian, W. Su, Failure analysis of convection section tube in an ethylene cracking furnace due to metal dusting, Engineering Failure Analysis 154 (2023) 107642. https://doi.org/10.1016/j.engfailanal.2023.107642

[19] T.L. Skovhus, R.B. Eckert, E. Rodrigues, Management and control of microbiologically influenced corrosion (MIC) in the oil and gas industry—Overview and a North Sea case study, Journal of biotechnology 256 (2017) 31–45. https://doi.org/10.1016/j.jbiotec.2017.07.003

[20] M.E.A.B. Seghier, B. Keshtegar, K.F. Tee, T. Zayed, R. Abbassi, N.T. Trung, Prediction of maximum pitting corrosion depth in oil and gas pipelines, Engineering Failure Analysis 112 (2020) 104505. https://doi.org/10.1016/j.engfailanal.2020.104505

[21] R.A. Bickham, Causes of High-Temperature Sulfidation in Refineries, Materials Performance 60(12) (2021) 14–16. https://doi.org/10.5006/MP2021_60_12-14

[22] M. Iannuzzi, A. Barnoush, R. Johnsen, Materials and corrosion trends in offshore and subsea oil and gas production, npj Materials Degradation 1(1) (2017) 2. https://doi.org/10.1038/s41529-017-0003-4

[23] S. Vishnuvardhan, A.R. Murthy, A. Choudhary, A review on pipeline failures, defects in pipelines and their assessment and fatigue life prediction methods, International Journal of Pressure Vessels and Piping 201 (2023) 104853. https://doi.org/10.1016/j.ijpvp.2022.104853

[24] M. Vakili, P. Koutník, J. Kohout, Addressing hydrogen sulfide corrosion in oil and gas industries: a sustainable perspective, Sustainability 16(4) (2024) 1661. https://doi.org/10.3390/su16041661

[25] M.D. Gunarathna, High-temperature Sulfidic Attack on Carbon Steel and Select Alloys, (2025). https://doi.org/10.11575/PRISM/48766

[26] I. Patel, G. Bota, D. Young, Mechanistic Insights into Refinery Sulfidation Corrosion, AMPP CORROSION, AMPP, 2023, pp. AMPP–2023–19107. https://doi.org/10.5006/C2023-19107

[27] T. Guo, X. Cao, H. Shao, Q. Zhao, Z. Liang, Effect of Fe on the oxidation, sulfidation and carburization behaviors of alloys in CO2 containing SO2, Corrosion Science 222 (2023) 111438. https://doi.org/10.1016/j.corsci.2023.111438

[28] M. Yousefi, M.H. Farghadin, A. Farzadi, Investigate the causes of cracks in welded 310 stainless steel used in the Flare tip, Engineering Failure Analysis 53 (2015) 138–147. https://doi.org/10.1016/j.engfailanal.2015.04.002

How to cite: Farghadin M.H, Nemati M, Mosayebi R. Investigation of Finned Tubes Failure in the Furnace of Dehydration Unit at 10th Refinery of South Pars Gas Complex. Journal of Chemical and Petroleum Engineering 2026; 60(1): 163-181.